

## Supplementary Information

### Origins of hydrogen peroxide selectivity during oxygen reduction on organic mixed ionic-electronic conducting polymers

Ana De La Fuente Durán<sup>1</sup>, Allen Yu-Lun Liang<sup>2</sup>, Ilaria Denti<sup>1</sup>, Hang Yu<sup>3</sup>, Drew Pearce<sup>3</sup>, Adam Marks<sup>1</sup>, Emily Penn<sup>4</sup>, Jeremy Treiber<sup>1</sup>, Karrie Weaver<sup>5</sup>, Lily Turaski<sup>1</sup>, Iuliana P. Maria<sup>6,7</sup>, Sophie Griggs<sup>7</sup>, Xingxing Chen<sup>8</sup>, Alberto Salleo<sup>1</sup>, William C. Chueh<sup>1</sup>, Jenny Nelson<sup>3</sup>, Alexander Giovannitti<sup>1,\*</sup>, J. Tyler Mefford<sup>1,\*</sup>

1. *Department of Materials Science and Engineering, Stanford University, Stanford, CA 94305, USA.*

2. *Department of Chemistry, Stanford University, Stanford, CA 94305, USA.*

3. *Department of Physics, Imperial College London, London SW7 2AZ, United Kingdom*

4. *Department of Chemical Engineering, Stanford University, Stanford, CA 94305, USA.*

5. *Department of Earth System Science, Stanford University, Stanford, CA 94305, USA.*

6. *Department of Chemistry, Imperial College London, London W12 0BZ, United Kingdom.*

7. *Department of Chemistry, Chemistry Research Laboratory, University of Oxford, Oxford OX1 3TA, United Kingdom.*

8. *Department of Materials, School of Chemistry and Chemical Engineering, Anhui University, Hefei 230601, Anhui, People's Republic of China.*

## **Supplementary Note 1: Hydrogen peroxide production**

Hydrogen peroxide has growing utilization as a green oxidant in industrial applications ranging from paper bleaching to environmental remediation.<sup>1-3</sup> Currently, H<sub>2</sub>O<sub>2</sub> is primarily produced via the thermochemical anthraquinone oxidation process,<sup>4</sup> which requires a high energy input and relies on fossil fuel-derived H<sub>2</sub>, high pressures, large volumes of organic solvents, and palladium catalysts, resulting in wastewater, exhaust gas, and solid waste.<sup>2</sup> Direct electrochemical reduction of oxygen to H<sub>2</sub>O<sub>2</sub> is a cost effective and energy efficient production pathway to reduce the environmental footprint of current industrial production.<sup>5</sup> Additionally, this method offers the possibility of distributed production at the points of use.

To enable electrochemical production, the activity and, more importantly, the selectivity of current electrocatalysts must be improved. Depending on the electrocatalyst, the oxygen reduction reaction (ORR) can yield two possible products: a 4-electron reaction that results in H<sub>2</sub>O, and a 2-electron reaction that produces H<sub>2</sub>O<sub>2</sub>. Most electrocatalysts that are considered state-of-the-art for the ORR are based on platinum-group metals, which, beyond being scarce and expensive, are predominantly selective for the 4-electron reaction.<sup>6</sup> Alternative directions include the development of non-precious, transition metal based electrocatalysts such as metal complexes,<sup>7,8</sup> metal oxides,<sup>9-11</sup> metal sulfides,<sup>12</sup> and single atom catalysts,<sup>13,14</sup> which may be selective for the 4-electron or the 2-electron reaction depending on their composition and structure. While these materials can achieve high activities in the ORR/HPPR, they face challenges with conductivity and are often not stable enough to provide an attractive alternative to thermochemical H<sub>2</sub>O<sub>2</sub> production.<sup>15</sup> For the HPPR, the most efficient heterogeneous electrocatalysts avoid metal sites entirely and include carbon nitrides, graphene derivatives, and other heteroatom-doped carbons capable of producing H<sub>2</sub>O<sub>2</sub> at overpotentials as low as 10 mV.<sup>16-19</sup> Still, these materials present their own challenges towards improving electrocatalyst design for this reaction, including the implausible identification of binding sites and mechanistic conclusions about their operation due to their variability in chemical structure.<sup>20,21</sup>

## Section 1. Polymer purification

### Purification process

A 5 mg ml<sup>-1</sup> solution of p(NDI-T2 P75) was prepared in chloroform, filtered through a 0.45 µm syringe filter and loaded onto the Recycling Preparative HPLC (LaboACE LC-5060) using a glass injection syringe. The polymer was cycled twice, the initial and final sections of the second cycle were separated from the main peak of cycle two (Figure S1). The major peak was collected, dried under reduced pressure then precipitated into methanol and finally filtered to afford the purified polymer.

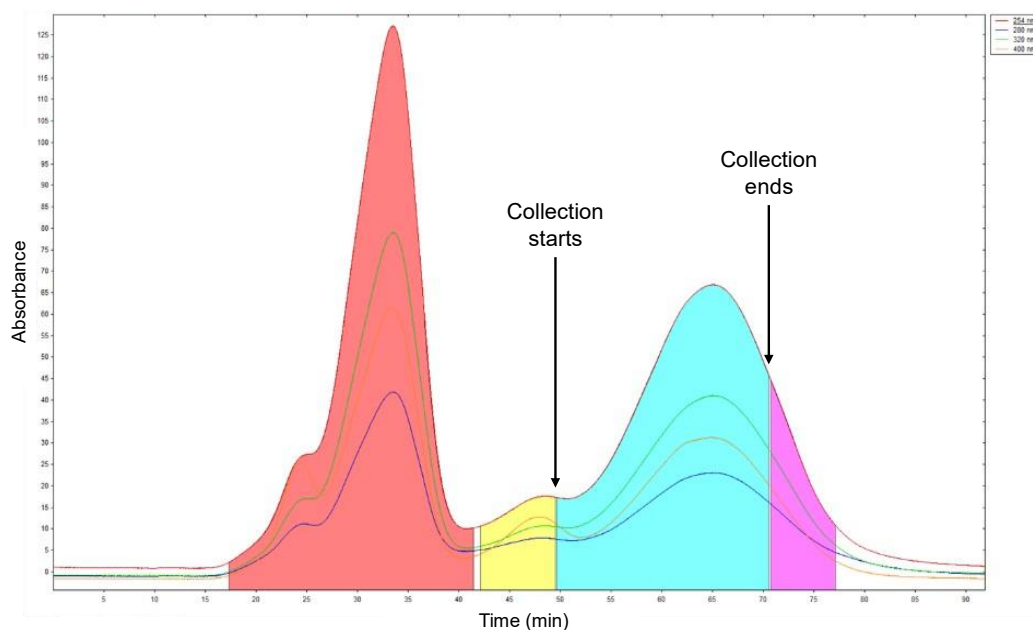


Figure S1. Purification of p(NDI-T2 P75) via gel permeation (GPC) chromatography. The first cycle of recycling is highlighted in red. The collected portion of the polymer is highlighted in cyan, and it corresponds to the main peak of the second recycling cycle.

### Quantifying Pd contamination through ICP-MS

Element concentrations were determined based on dry polymer weight. Samples were digested in TraceMetal® grade (Fisher Scientific) concentrated nitric acid under elevated temperature (200 °C) and pressure in fluoropolymer pressure vessels in a CEM MARS5 microwave digestion system. Digested sample solutions were clear with no undissolved material or precipitates. Digested samples were diluted with 2% v/v nitric acid prior to analysis to target an estimated 1-100 µg L<sup>-1</sup> in the analytical solution.

Analysis was performed on an Agilent 8900 ICP-MS attached to an Agilent SPS-4 autosampler. The sample introduction system also includes a standard Scott double pass cooled spray chamber operated at 2 °C, a 2.5mm i.d. Agilent glass torch, and a 200 µl min<sup>-1</sup> Micromist nebulizer. The ICP-MS was fitted with standard nickel cones and operated in no gas mode.

Before analysis, all solutions were further diluted by 50% by adding an internal standard solution of  $2 \mu\text{g L}^{-1}$  platinum and rhodium (High Purity Standards) prepared with 2% v/v nitric acid to correct for instrumental drift. Procedural blanks were run in parallel with samples and averaged 14 ng contributing to less than 2% of the analytical signal and are regarded as negligible. Reproducibility is estimated to be 2.8% RSD from repeated analyses ( $n = 11$ ) over 2 analytical sessions of an in-house QC sample prepared from a polymer of known Pd composition.

**Table S1. Pd concentration in polymer samples before and after purification.**

Sample	Pd concentration (ppm)
p(NDI-T2 P75), Purified, Pd added	~230,000
p(NDI-T2 P75), Unpurified	5730
p(NDI-T2 P75), Purified	2-5
p(NDI-T), Purified	63
p(gPyDPP-MeOT2), Purified	10
p(g3T2), Purified	182
N2200, Unpurified	520

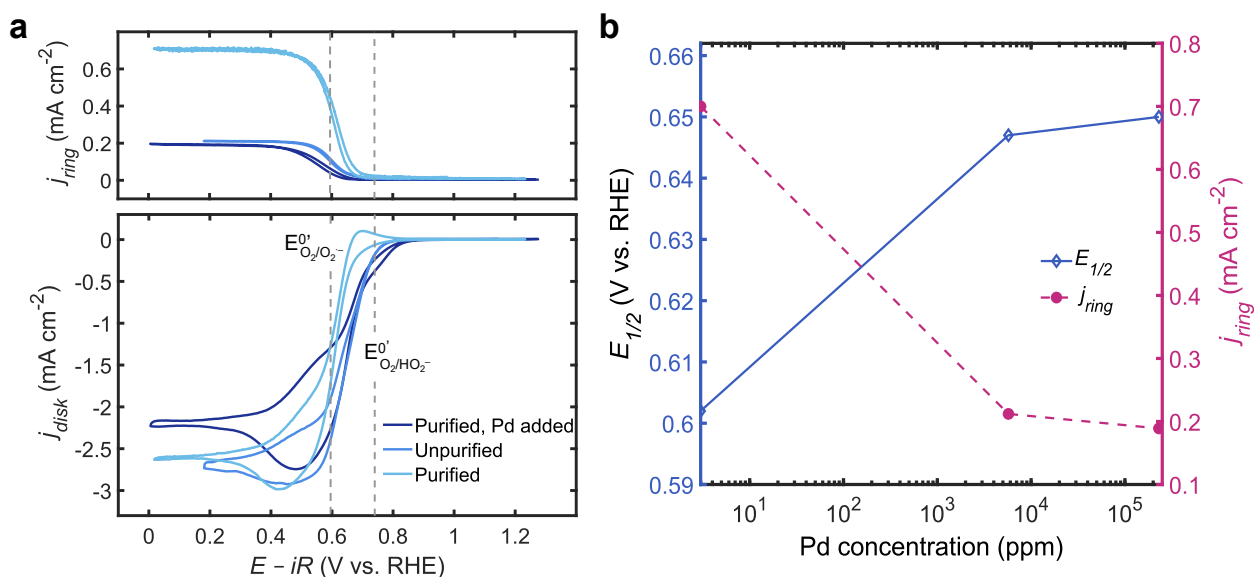


Figure S2. Electrochemical performance changes due to Pd concentration. a) RRDE measurements in 0.1 M KOH at 1600 r.p.m. with a scan rate of  $5 \text{ mV s}^{-1}$  for samples with differing Pd concentrations (see Table S1). b) Halfwave voltages (blue) and ring current densities (magenta) as a function of Pd concentration.

## **Section 2. Additional electrochemical measurements on p(NDI-T2 P75)**

### *Organic electrochemical transistor testing*

#### *Methods*

For the organic electrochemical transistor device measurements, p(NDI-T2 P75) interdigitated array microelectrodes (10/10  $\mu\text{m}$ , electrode/gap, Micrux Technologies) were cleaned by sonicating the devices in acetone and isopropanol for 15 min. Thin films of p(NDI-T2 P75) were prepared by spin coating (1000 RPM, 1 min). The excess p(NDI-T2 P75) not directly on the interdigitated electrode was removed by wiping off the polymer with acetone and the areas of the device was measured with a profilometer (general film thickness was on the order of 200 nm). The interdigitated electrodes were contacted by soldering wires onto each electrode (1.0 mm diameter, Cerasolzer, Alloy #GS155, MBR Electronics). To prevent the exposed gold of the interdigitated electrodes and the metal of the soldered wires from contacting solution, they were both covered in epoxy (5 minute setting, Loctite Epoxy). The interdigitated electrode was then loaded into an electrolyte-gated transistor cell with a 0.2  $\text{cm}^2$  exposed area (components made from PEEK and glass, sealed with EPDM O-rings, redox.me, Electrolyte-Gated Transistor BMM Cell). The cell was filled with 10 mL of 0.1 M KCl or 0.1 M KOH and was used with a PEEK-shrouded leakless Ag/AgCl reference electrode (eDAQ) and a coiled Pt wire counter electrode. Measurements were completed using a WaveDriver 200 bipotentiostat (Pine Research) in Ar-saturated and  $\text{O}_2$ -saturated electrolyte. Each working electrode was cycled between 0.2 V and  $-0.5$  V vs Ag/AgCl at  $5 \text{ mV s}^{-1}$  with an offset of 10 mV between the working electrodes.

#### *Results*

The reductive charging of NDI-T2 in the 0.2 V and  $-0.5$  V vs Ag/AgCl voltage window results in roughly one charge per polymer repeat unit, i.e. an “electron polaron”. As is evident in Figure S1c, the formation of the polaron leads to an increase in conductivity by 3-4 orders of magnitude, verifying the “n-type” behavior of the polymer and demonstrating control over conductivity through applied voltage.

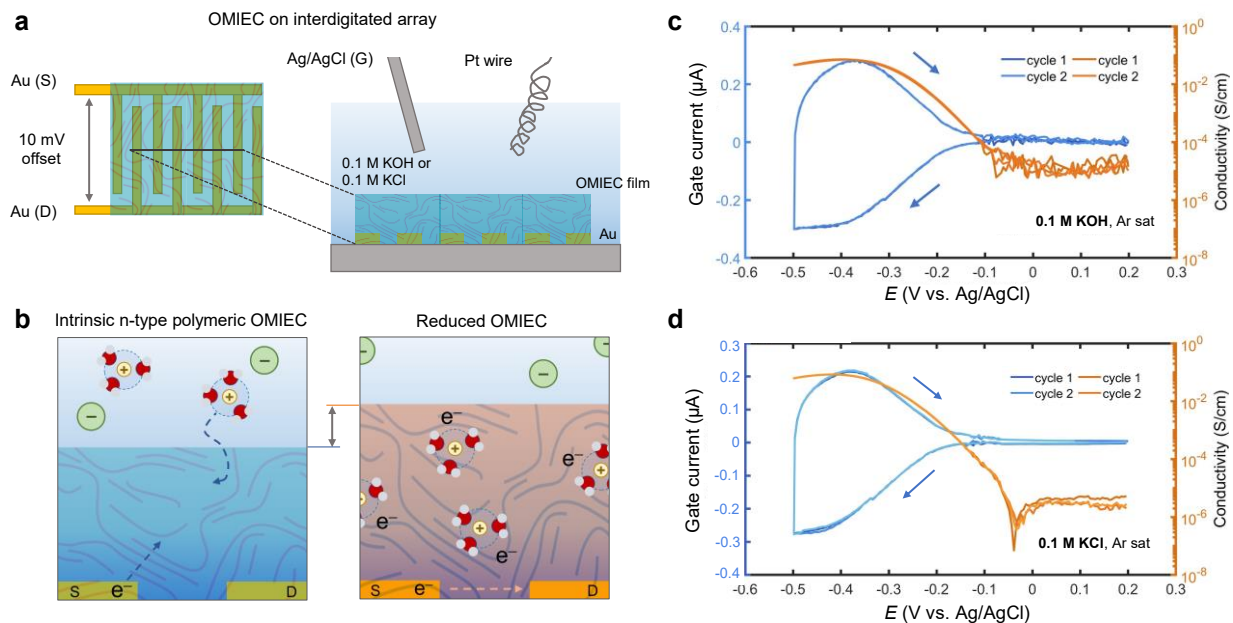


Figure S3. Conductivity measurements and reduction schematic for p(NDI-T2 P75). a) Schematics of an interdigitated array electrode subsequently placed in 0.1 M KOH (or 0.1 M KCl) aqueous solution and operated as an OECD device. b) Depiction of the coupled processes of electron injection and solvated-cation insertion in an OMIEC film reduced in Ar-saturated solution, resulting in mobile electrons and an increase in thickness due to swelling. Gate currents and conductivities measured as p(NDI-T2 P75) is reduced and oxidized (negative and positive sweep directions, respectively) in Ar-saturated c) 0.1 M KOH solution and d) 0.1 M KCl solution. In both electrolytes, conductivity increases by 3-4 orders of magnitude as the polymer is reduced.

## Mass loading experiments

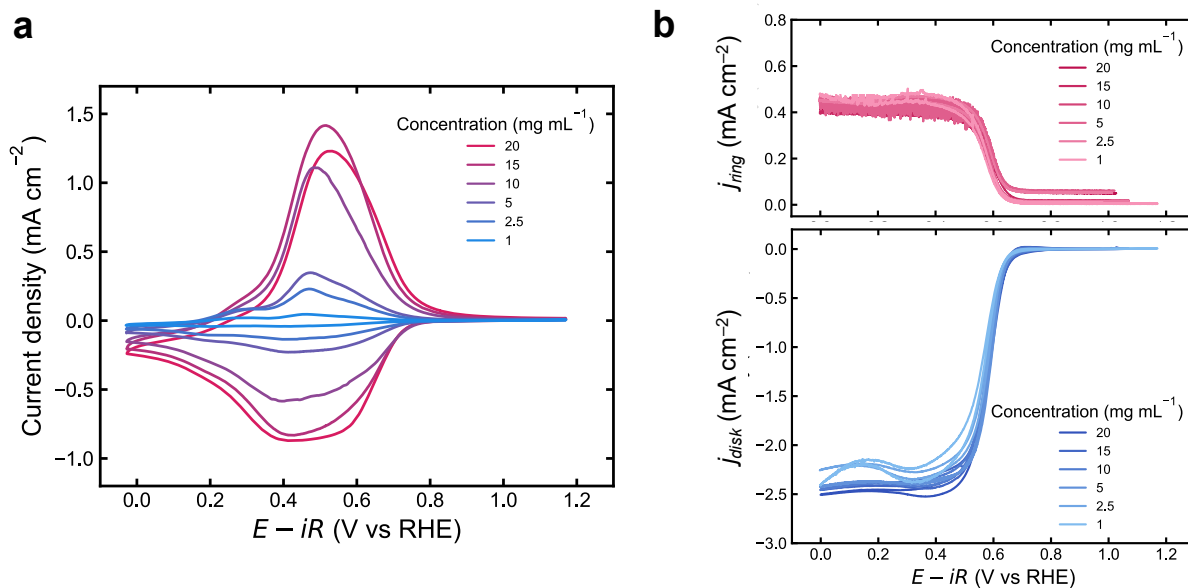


Figure S4. Mass loading measurements for p(NDI-T2 P75) in 0.1 M KOH. p(NDI-T2 P75) was dissolved in chloroform to prepare solutions ranging in from 1 to 20  $\text{mg mL}^{-1}$  in concentration. 10  $\mu\text{L}$  of each solution were used to drop cast electrodes. a) Ar-saturated reduction/oxidation voltammograms at a scan rate of  $5 \text{ mV s}^{-1}$ . b)  $\text{O}_2$ -saturated RRDE measurement at 1600 r.p.m. with a scan rate of  $0.5 \text{ mV s}^{-1}$ , showing a high ring current ( $E_{\text{ring}} = 1.20 \text{ V vs. RHE}$ ).

### Koutecký-Levich measurements for all pH

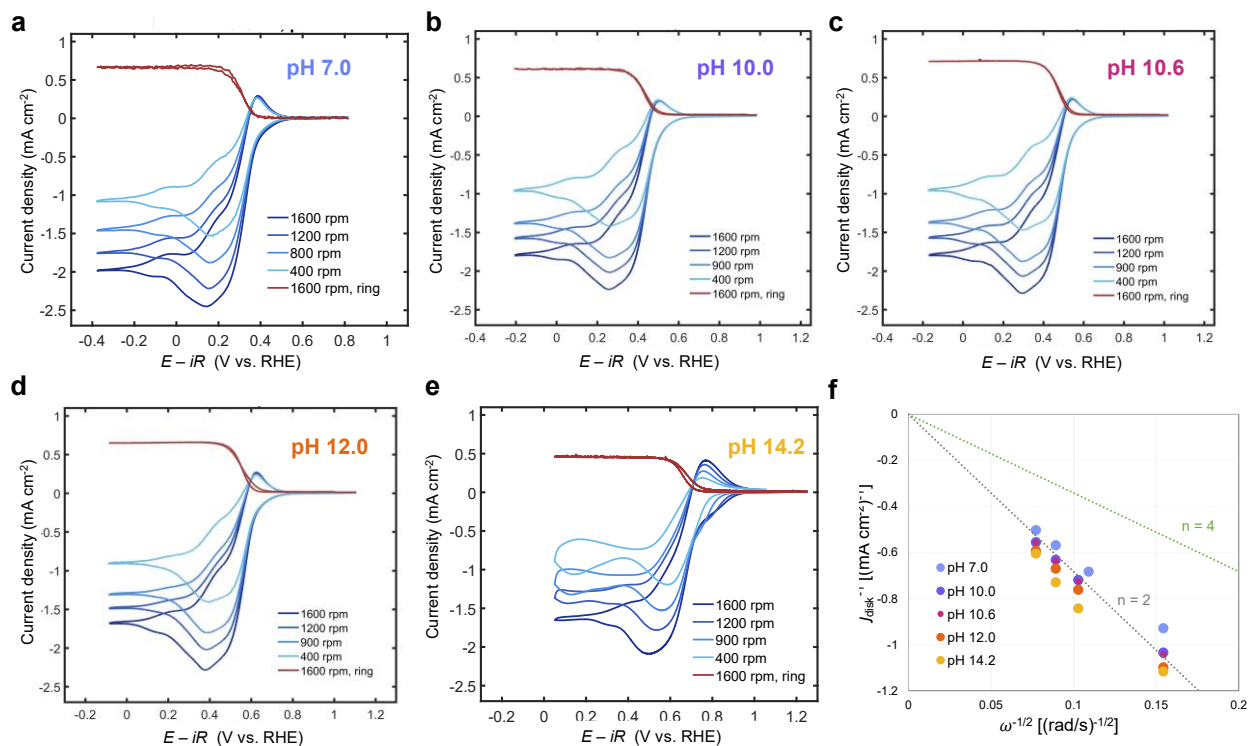


Figure S5. Koutecký-Levich measurements for p(NDI-T2 P75). ORR measurements performed at electrode rotation speeds of 1600, 1200, 900, and 400 r.p.m. a scan rate of 5 mV s<sup>-1</sup> in [K<sup>+</sup>] = 1 M aqueous electrolytes with pH a) 7.0, b) 10.0, c) 10.6, d) 12.0, and e) 13.7. f) Koutecký-Levich plot for the experiments displayed in a-e. The current density values used were taken at -0.9 V vs Ag/AgCl. The slopes of the fitted lines for each pH were used to calculate the number of electrons transfer to O<sub>2</sub>,  $n$ , according to the Koutecký-Levich equation.

### Section 3. Platinum electrochemical measurement comparisons

Koutecký-Levich measurements for all pH

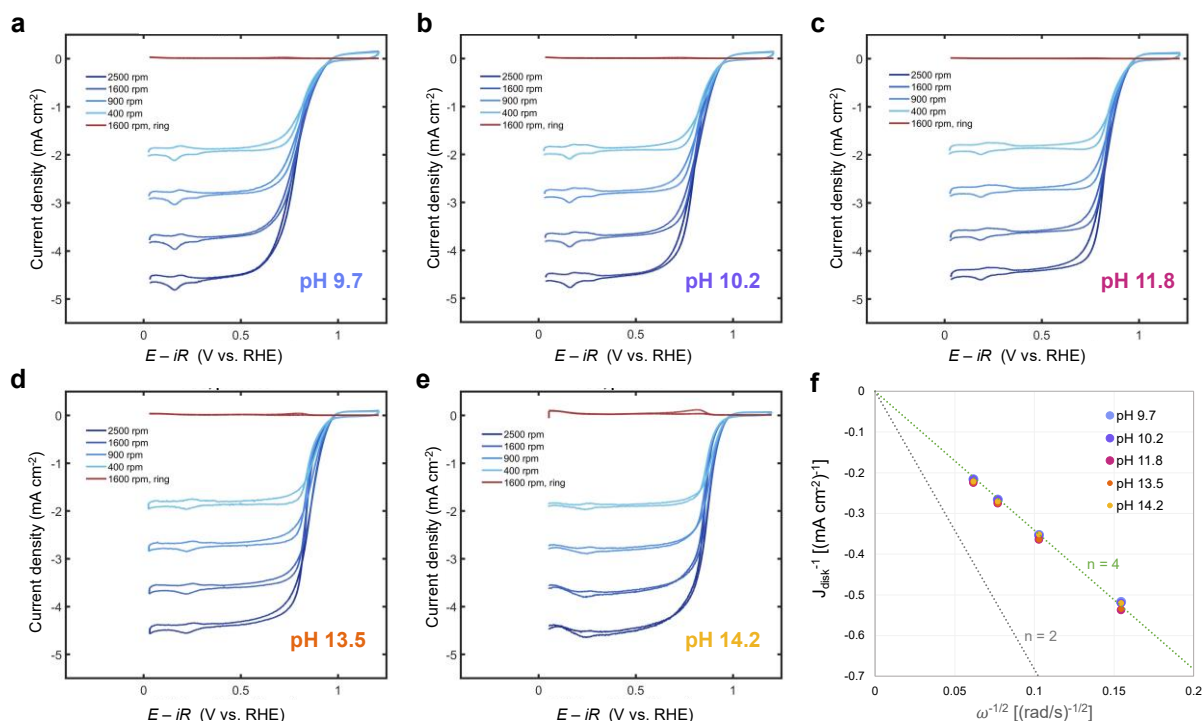


Figure S6. Koutecký-Levich measurements for polycrystalline Pt. ORR measurements performed at electrode rotation speeds of 2500, 1600, 900, and 400 r.p.m. at a scan rate of 5 mV s<sup>-1</sup> in [K<sup>+</sup>] = 1 M aqueous electrolytes with pH a) 9.7, b) 10.2, c) 11.8, d) 13.5, and e) 14.2. f) Koutecký-Levich plot for the experiments displayed in a-e. The used current density values were taken at -0.9 V vs Ag/AgCl. The slopes of the fitted lines for each pH were used to calculate the number of electrons transfer to O<sub>2</sub>, *n*, according to the Koutecký-Levich equation.

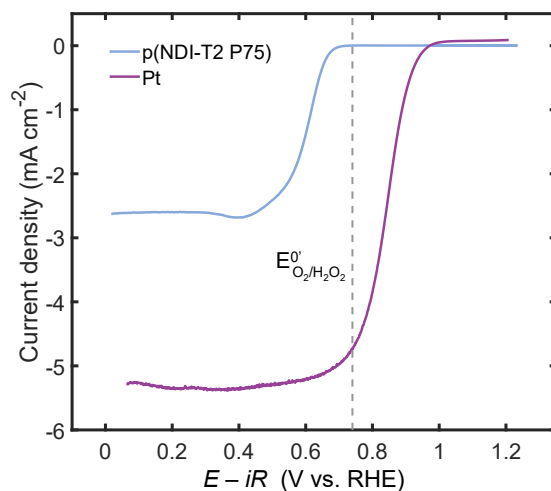


Figure S7. Comparing p(NDI-T2 P75) ORR performance to polycrystalline Pt. ORR measurements performed at 1600 r.p.m. at a scan rate of 5 mV s<sup>-1</sup> in 0.1 M KOH solution. The p(NDI-T2 P75) data is the average of the forward and backward scans.

## Section 4. Chemical structure characterization

### XPS methods

XPS spectra were obtained on polymer samples drop cast from a solution of p(NDI-T2 P75) dissolved in chloroform ( $\sim 10 \text{ mg mL}^{-1}$ ) on glassy carbon electrodes. To create thick polymer films (estimated thickness =  $1 \mu\text{m}$ ),  $10 \mu\text{L}$  of this solution was dropcast onto the glassy carbon disk of a rotating ring disk electrode (RRDE). Two types of samples were analyzed: an untested, pristine polymer and a post-test polymer to determine whether polymer samples notably degrade after a 24-hour constant current electrolysis measurement. XPS data was obtained using a PHI VersaProbe 4 X-ray photoelectron spectrometer using a monochromatized Al(K $\alpha$ ) source with a spot size of  $200 \mu\text{m}$ . The detector was positioned at  $45^\circ$  and data was obtained using  $55 \text{ eV}$  pass energy with  $0.1 \text{ eV}$  step resolution. Data was smoothed with a 5-point, 3rd degree polynomial utilizing the Savitzky-Golay method and peaks were fitted with Gaussian-Lorentzian functions using CasaXPS software. The binding energy of each element was shifted by setting the adventitious carbon peak at  $284.8 \text{ eV}$ .

### XPS results

XPS data show that the pristine and post-test samples are compositionally similar. Integrating peak areas shows that there is a maximum change of 11% in an element's atomic concentration relative to C 1s. This is within the bounds of experimental and fitting errors. There are no significant shifts in binding energies that would provide evidence for the formation of new chemical species. It is unlikely that the polymer surface, which we have shown is the active region for oxygen reduction, experiences large chemical changes upon being operated at a constant current density of  $-2 \text{ mA cm}^{-2}$  in during oxygen reduction in  $0.1 \text{ M KOH}$ .

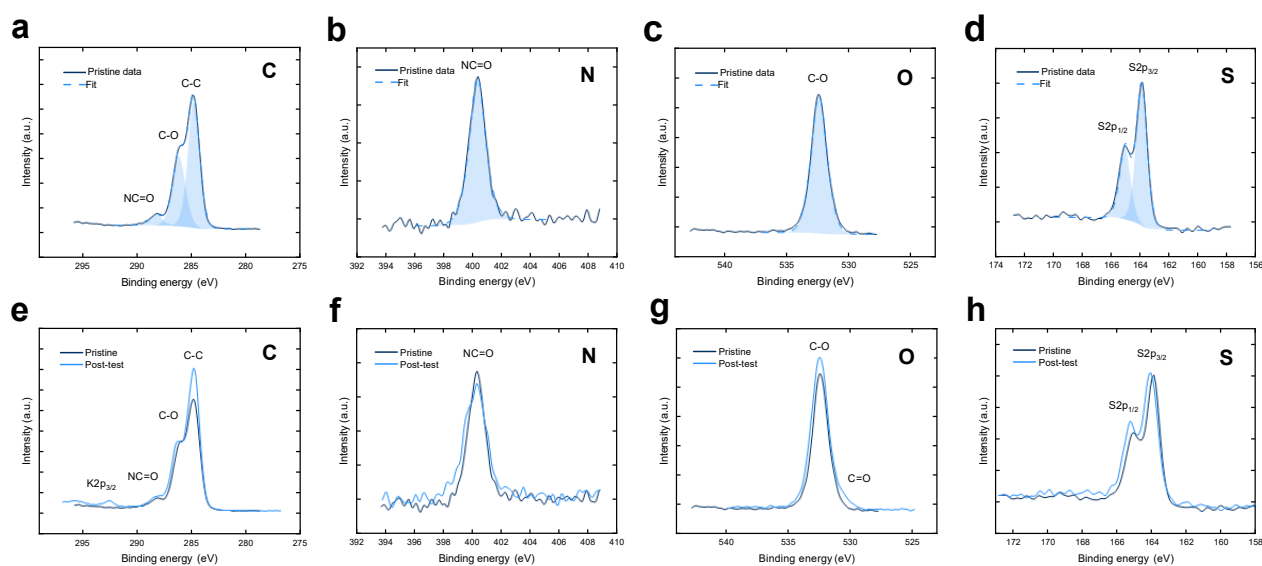


Figure S8. XPS spectra of polymer samples drop cast on glassy carbon electrodes. (a-d) Fitted data is plotted against the pristine sample spectra. Integration of the fitted peaks is used to

determine relative element concentrations in each sample. (e-h) Pristine sample data is plotted against the post-test data. Spectra show that there is minimal change in composition between the pristine sample and the post-test sample. All peaks can be accounted for in each sample based on the polymer's molecular structure. Notably, the peak locations are nearly identical which signifies that the chemical environment of the polymer after 24-hour constant current electrolysis is unchanged.

### *NMR methods*

Two polymer solutions were prepared in deuterated chloroform to investigate the chemical stability of p(NDI-T2 P75) using  $^1\text{H}$  NMR spectroscopy before and after electrochemical testing in alkaline aqueous electrolytes. The first sample contains the neat polymer dissolved in deuterated chloroform ( $2\text{ mg mL}^{-1}$ ). The second polymer sample contains a polymer solution ( $2\text{ mg mL}^{-1}$ ) of the electrochemically tested polymer. Electrochemical stability measurements were carried out on a  $4\text{ mg cm}^{-2}$  p(NDI-T2 P75) electrode on carbon fiber paper (AvCarb P50T, Fuel Cell Store) prepared through drop-casting from a  $2\text{ mg mL}^{-1}$  ink of the polymer in chloroform. Potentiostatic electrolysis was performed in  $\text{O}_2$ -saturated  $0.1\text{M KOH}$  in an H-cell at  $-0.5\text{ V}$  vs.  $\text{Ag/AgCl}$  for two hours. After the electrochemical measurement has been completed, the electrode was washed with DI water and dried in inert conditions. The polymer was re-dissolved by placing the dried polymer carbon electrode in deuterated chloroform and sonicating for 5 min. The  $^1\text{H}$  NMR spectrum was collected and compared to the neat polymer.

NMR results

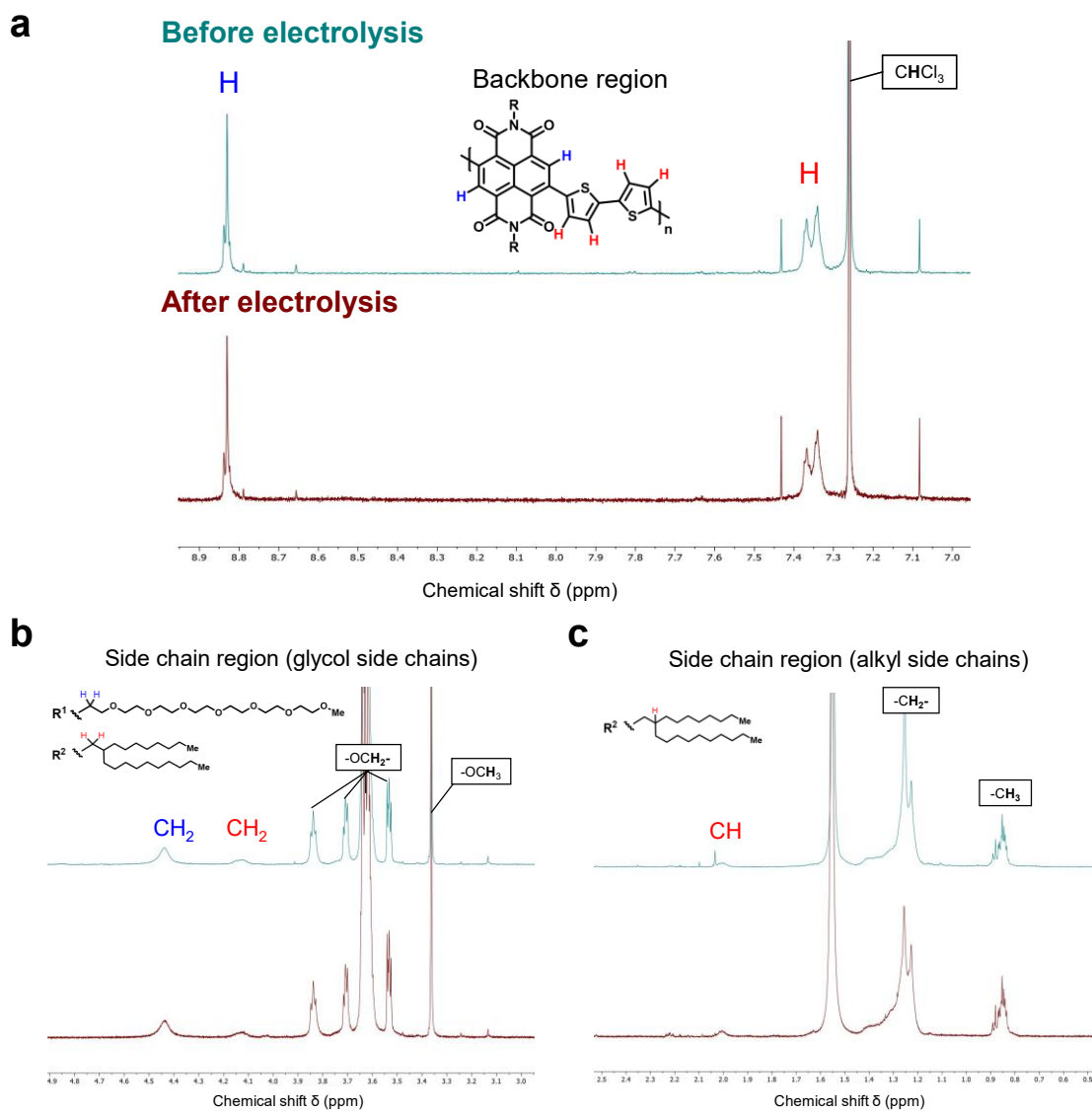


Figure S9.  $^1\text{H}$  NMR spectra for samples of p(NDI-T2 P75) before and after the constant current electrolysis experiments performed in an H-cell, showing a) the backbone region, b) the glycol side chain region, and c) the alkyl side chain region.

## **Section 5. Scanning electron microscopy characterization**

### *Methods*

To assess any potential changes in morphology, we prepared two samples for SEM characterization. Both samples were prepared by drop casting p(NDI-T2 P75) on carbon paper with a loading of  $1 \text{ mg cm}^{-2}$ . One sample was imaged in a pristine, untested state. The other sample was imaged after being used for the 25-hour constant  $-2 \text{ mA cm}^{-2}$  current electrolysis measurement in the small volume H-cell. The SEM characterization was conducted using an FEI Magellan 400 XHR Scanning Electron Microscope with an acceleration voltage of 5.0 kV and beam current of 25 pA.

### *Results*

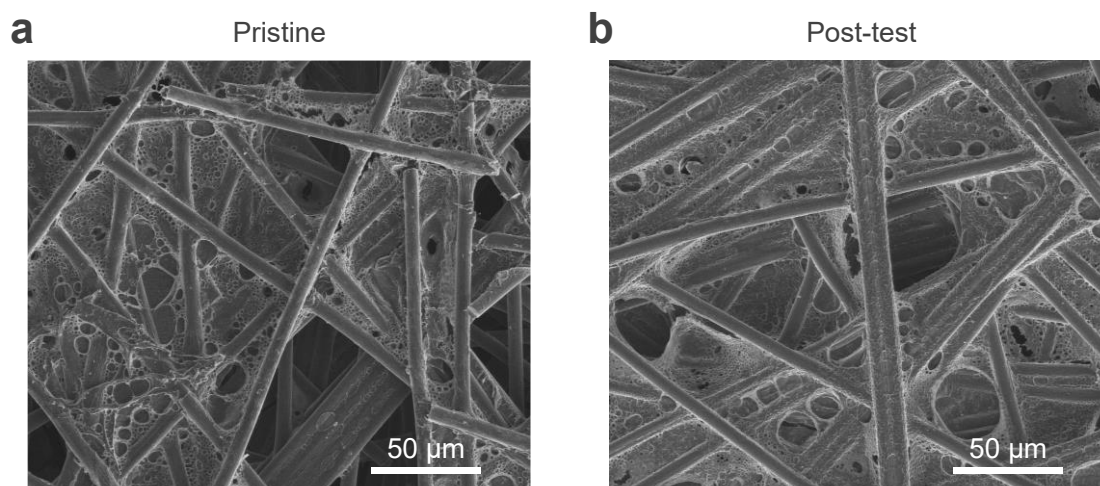


Figure S10. SEM images of samples of p(NDI-T2 P75) on carbon paper in a) a pristine, untested state and b) after 25-hour constant current electrolysis. Both samples show p(NDI-T2 P75) in the same sort of netted morphology spanning between the rigid fibers of the carbon paper. No notable changes in morphology are observed between the pristine and post-test samples.

## Section 6. pH dependence for redox processes and oxygen reduction

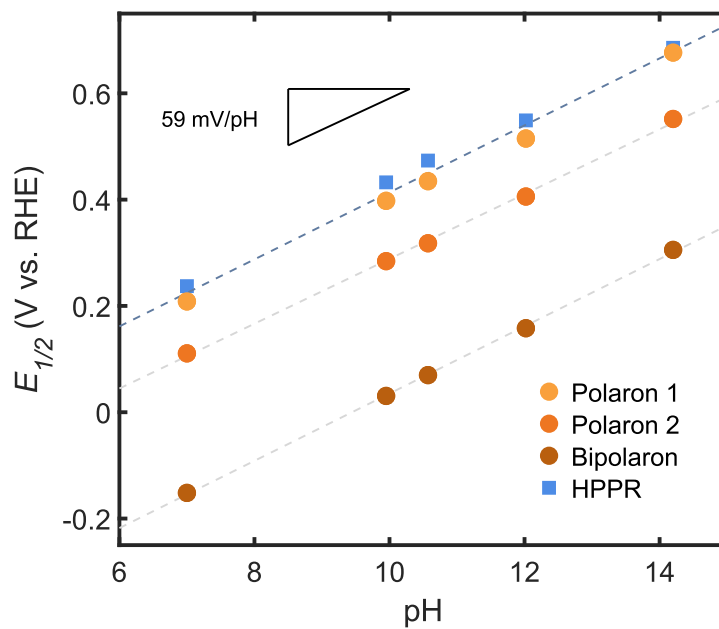


Figure S11. Halfwave voltage,  $E_{1/2}$ , for the different redox peaks seen in cyclic voltammograms and oxygen reduction (HPPR) vs. pH.

## Section 7. Spectroscopic characterization of p(NDI-T2 P75) in 0.1 M KCl

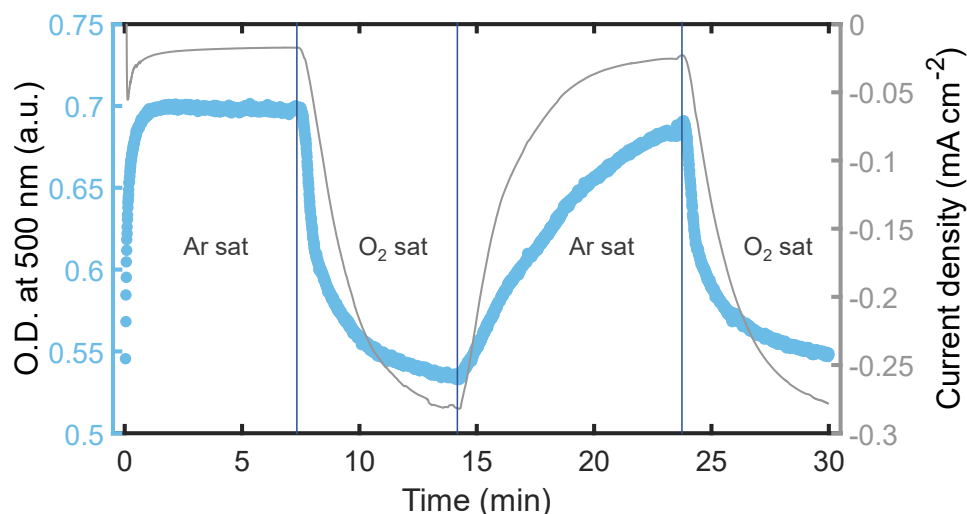


Figure S12. UV-Vis spectroelectrochemistry of a thin p(NDI-T2 P75) film on indium tin oxide (ITO) glass in 0.1 M KCl. Changes in optical density at 500 nm are tracked as the potential is held at  $-1.0$  V vs Ag/AgCl while the electrolyte fed into the flow cell is changed between Ar-saturated and  $O_2$ -saturated to track the appearance and disappearance of the electron polaron.

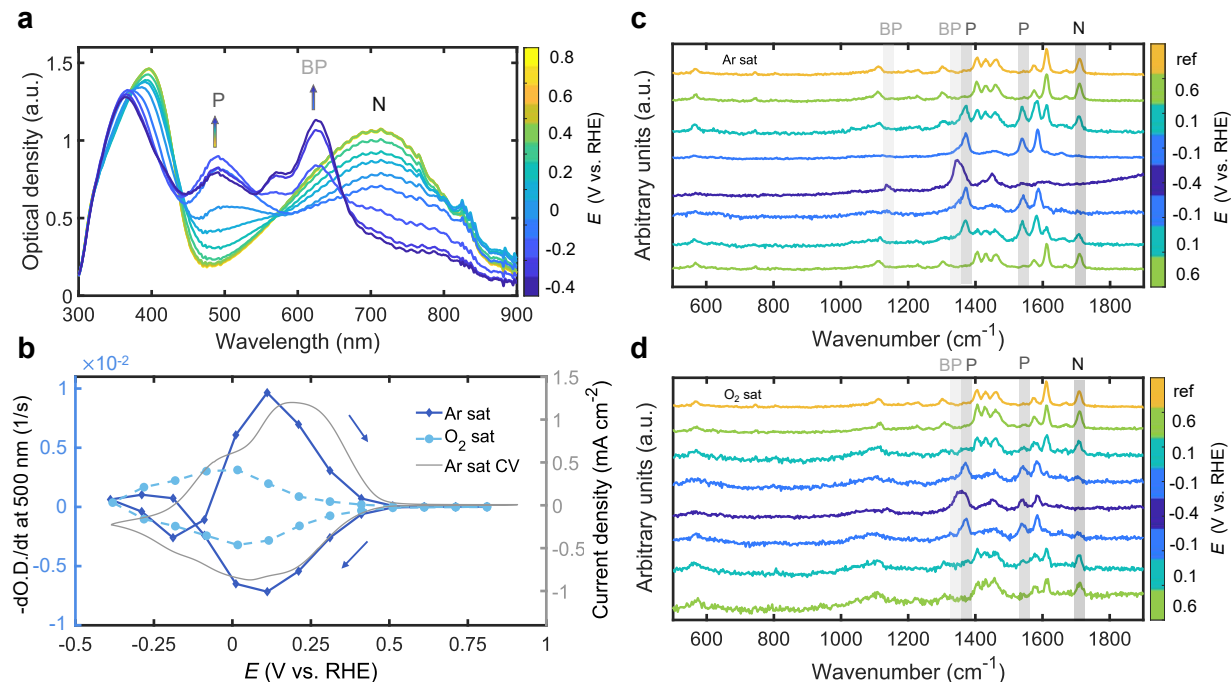


Figure S13. *Operando* spectroscopy of thin films of p(NDI-T2 P75) during ion-insertion redox reactions. a) UV-Vis spectra of a thin p(NDI-T2 P75) film on indium tin oxide (ITO) glass as it is electrochemically reduced in Ar-saturated 0.1 M KCl to its doubly-reduced, bipolaron state. N indicates the absorption peak associated with the neutral state of the polymer, P indicates the

electron polaron peak, and BP indicates the bipolaron peak. b) Negative change in optical density at 500 nm with respect to time for Ar-saturated and O<sub>2</sub>-saturated 0.1 M KCl as the polymer is reduced to its electron bipolaron state, demonstrating the suppression of electron polaron formation. The CV was collected in 0.1 M KCl at 5 mV s<sup>-1</sup>. c) *Operando* Raman spectra for a thin p(NDI-T2 P75) film on ITO glass as it is electrochemically reduced and oxidized in Ar-saturated 0.1 M KCl. From darkest to lightest grey, the vibrational mode(s) highlighted are indicative of the neutral state (N) of the polymer, the electron polaron (P), and the electron bipolaron (BP), respectively. d) *Operando* Raman spectra for a thin p(NDI-T2 P75) film on ITO glass as it is electrochemically reduced and oxidized in O<sub>2</sub>-saturated 0.1 M KCl. Like the UV-Vis results, the electron polaron is suppressed in the presence of O<sub>2</sub> while the bipolaron is limitedly observed.

In both 0.1 KOH and 0.1 M KCl *operando* Raman experiments, no new features were observed in O<sub>2</sub>-saturated electrolyte that could be explained through a surface bound oxygen intermediate. O-O stretching modes for superoxide adsorbates on metals have been reported in the range of ~1000 – 1200 cm<sup>-1</sup>,<sup>22-27</sup> which overlaps with one of the neutral p(NDI-T2 P75) Raman modes and, as such, cannot be unequivocally ruled out. However, there is no apparent intensity increase in this region during ORR. Surface bound peroxides have stretching modes at lower wavenumbers, from 640 – 900 cm<sup>-1</sup>,<sup>22,28,29</sup> and we observe no increased Raman intensity in this region. However, we note the expected intermediates for oxygen reduction would be confined to the OMIEC/electrolyte interface if they were present, which would result in a relatively low volumetric adsorbate density and would make their detection difficult without implementing additional signal enhancement measures.

## Section 8. Extended quantum chemical calculations

### Methods

Molecules in their neutral and singly reduced (electron polaron) states were optimized using density functional theory (DFT) with B3LYP/6-311+g(d,p) level of theory in a water environment (Solvation Model Based on Density, SMD). The charge distributions of the molecules in the two states with optimized structures were calculated using the CHELPG scheme (Charge from Electrostatic Potentials using a Grid-based method). The additional charge distributions were then calculated via  $Q_{add.} = Q_{red.} - Q_{neu.}$  for each atom. All the quantum chemical calculations were performed in Gaussian 16, with GaussView 6.0.16 to build the molecules and visualize the calculation results.

In order to reproduce the reaction between p(NDI-T2 P75) and O<sub>2</sub> molecules and minimize the calculation complexity, an (NDI-T2) monomer with ethyl side chains and an O<sub>2</sub> molecule were used in the calculation (Figure S10). The two molecules are either optimized separately (isolated NDI-T2, (NDI-T2), and isolated O<sub>2</sub>, (O<sub>2</sub>)) or optimized together as a complex, (NDI-T2 + O<sub>2</sub>). In the latter case, four potential reaction sites were considered, i.e. C4a1, C4a2, N and S as marked pink in Figure S14. The system is optimized either in the neutral state or constrained to carry a total charge of  $-1 e^-$ . Before optimization, the O<sub>2</sub> molecule was placed with its axis perpendicular to the NDI plane with the perigee O atom 1.6 Å away from the reaction site in question. A starting distance of 1.2 Å was also tested, but our confidence in the calculations where O<sub>2</sub> was initialized so close to the monomer were lower. The total energy of the system, atomic positions and partial charge distribution after optimization are recorded.

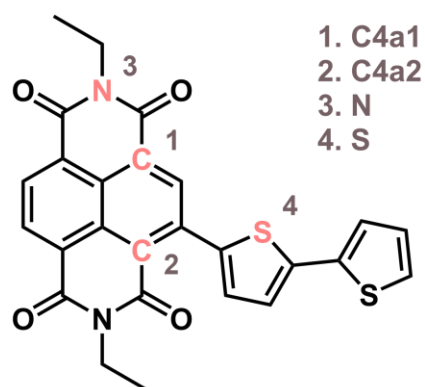


Figure S14. Chemical structure of the (NDI-T2) monomer that was used for the calculation. The four potential reaction sites are marked in red.

## Results

Figure S13 shows the total energy that was calculated for five neutral systems, where NDI-T2 and  $O_2$  were optimized separately or together, and six singly reduced systems, where the negative charge is carried by the isolated NDI-T2 or the isolated  $O_2$  (isolated (NDI) + ( $O_2$ )) or the complex ((NDI-T2 +  $O_2$ ) complex). Energies are plotted relative to that of the neutral separated pair. In the neutral states, the separated pair, (NDI-T2) + ( $O_2$ ), shows similar total energy to the (NDI-T2 +  $O_2$ ) complex, though the complex is stabilized slightly when  $O_2$  is located close to C4a2 or S (bithiophene) compared to the other positions (Figure S15a). For the reduced states, the reduced complex and the case where the  $O_2$  bears the entire charge are energetically favorable compared to the case where the NDI-T2 bears the charge. Inspection of the partial charge distribution for the reduced complex (Figure 5c) shows that the extra  $-1 e^-$  charge is mainly localized on the  $O_2$  leaving the NDI-T2 monomer almost neutral, irrespective of the  $O_2$  location in the complex (Figure 5d). The similarity in the energies across the different complexes, also suggests that the potential energy surface is probably very flat for different spatial separations of  $O_2$  and monomer in the reduced state (Figure S15b). This suggests that the lowest energy complex is similar in its nature to the case where the electron is fully transferred to an isolated  $O_2$ , and that the  $O_2$  is not strongly bound to the NDI-T2.

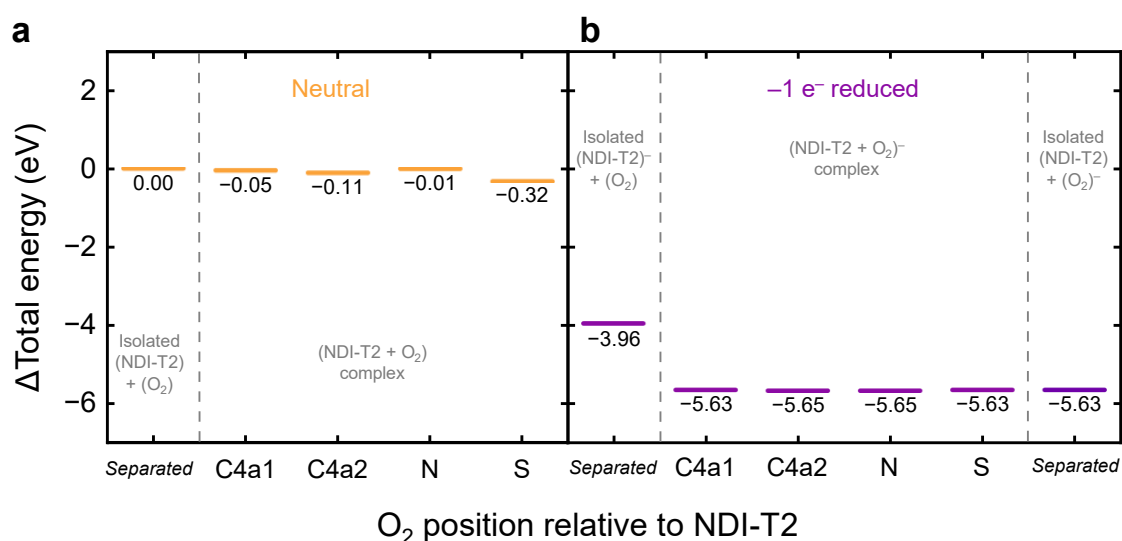


Figure S15. The DFT calculations show the total energy change of the neutral and the reduced (NDI-T2 +  $O_2$ ) complex against the total energy of the separated neutral pair (NDI-T2) plus ( $O_2$ ). **a)** Both NDI-T2 and  $O_2$  molecules are in neutral states.  $O_2$  does not show an affinity to bind to any of the potential tested binding sites. **b)** For the isolated (NDI-T2) $^-$  + ( $O_2$ ) separated case, the NDI-T2 was charged with an electron, while  $O_2$  was calculated separately in a neutral state; for the isolated (NDI-T2) + ( $O_2$ ) $^-$  separated case, the  $O_2$  was charged with an electron, whilst the

NDI-T2 was calculated separately in a neutral state; for the other cases, the (NDI-T2 + O<sub>2</sub>) complexes were reduced. No energetic preference is shown for the NDI-T2 to bear any of the added electron charge in the tested complex cases.

We note here that the energies of reduced systems containing O<sub>2</sub> may be underestimated by 1 eV or more due to the known difficulty in calculating reduced O<sub>2</sub> energy using DFT.<sup>30</sup> While this may affect the relative energy of the states with reduced O<sub>2</sub>, it would not change the similarity of the energies of the reduced complex and the separated (NDI-T2) + (O<sub>2</sub><sup>-</sup>) case, nor would it change the result that these two states are still the lowest states of the system. If we make the assumption that the DFT-calculated reduction potential of all complexes containing O<sub>2</sub> are offset by a certain amount while that of the monomer alone is correct, we would still find that the reduced (monomer plus O<sub>2</sub>) complex is more stable than the reduced monomer with a distant neutral O<sub>2</sub>. In other words, electron transfer from monomer to O<sub>2</sub> would still occur and the reduced complex where O<sub>2</sub> is initialized close to the monomer would still be more stable than the isolated reduced monomer and neutral O<sub>2</sub>. It should also be noted that the absolute energies calculated for the different states will be affected by the choice of DFT functional and basis set, yet B3LYP/6-311+g(d,p) has been demonstrated to calculate reasonable redox voltages for other (notably p-type) OMIECs.<sup>31</sup>

## **Supplementary Note 2. Calculating formal reduction potential for superoxide formation**

At pH > 4.88 (pK<sub>a</sub> of HO<sub>2</sub>), the first reduction of oxygen yields the superoxide radical, O<sub>2</sub><sup>-</sup>, as shown in Reaction [1]:



The standard reduction potential for this reaction is  $E_{\text{O}_2/\text{O}_2^-}^0 = -0.33 \text{ V vs. SHE}$ .<sup>32</sup> However, this potential corresponds to a superoxide activity of 1. In contrast, its formal reduction potential,  $E^0$ , can be calculated as follows, where  $R$  is the ideal gas constant,  $T$  is the absolute temperature,  $p_{\text{O}_2}$  is the partial pressure of O<sub>2</sub>, and  $a_j$  is the activity of species  $j$  in the aqueous solution:

$$E_{\text{O}_2/\text{O}_2^-}^{0'} (\text{V vs. SHE}) = E_{\text{O}_2/\text{O}_2^-}^0 + \frac{RT}{F} \ln \frac{p_{\text{O}_2}}{a_{\text{O}_2^-}} \quad [2]$$

The low stability of superoxide suggests that its concentration is unlikely to exceed the concentration of dissolved O<sub>2</sub> in the electrolyte from which it is produced. Although O<sub>2</sub> solubility is pH-dependent,<sup>33</sup> we can estimate the superoxide and oxygen activity through Henry's Law where the Henry's Law Constant for O<sub>2</sub> in water is  $H_{\text{O}_2}^{aq} = 1.3 \times 10^{-3} \text{ M atm}^{-1}$ :

$$a_{\text{O}_2^-} \approx a_{\text{O}_2} = H_{\text{O}_2}^{aq} p_{\text{O}_2} \quad [3]$$

Using this value for  $a_{\text{O}_2^-}$  we obtain a formal reduction potential of  $E_{\text{O}_2/\text{O}_2^-}^{0'} = -0.16 \text{ V vs. SHE}$ , which defines the reversible potential of dissolved oxygen reduction to superoxide in aqueous electrolytes.<sup>34,35</sup> We note this value corresponds well with commonly observed halfwave voltages ( $E_{1/2}$ ) on carbon-based electrodes in aqueous electrolytes.<sup>36</sup>

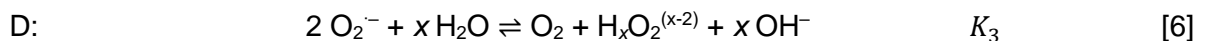
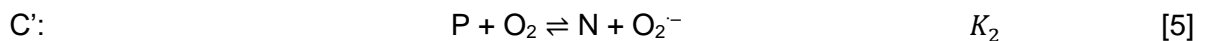
## **Section 9. Extended microkinetic model results**

### *Microkinetic model*

As discussed in the main text, there are three key observations regarding the performance of p(NDI-T2 P75) that can guide the informed selection of an oxygen reduction mechanism. First, through *operando* spectroscopy measurements, we observe that the formation of the reduced (bi)polaron state in the polymer is suppressed but do not observe an adsorbed intermediate. This points towards a chemical reaction in which an electron is transferred between the polaronic state of the polymer and an oxygen reduction intermediate forming a reduced oxygen species and re-oxidizing the polymer to the neutral state in the process. Second, we find that the observed halfwave voltages,  $E_{1/2}$ , for oxygen reduction on p(NDI-T2 P75) across the investigated pH range correspond well with the reversible voltage for the single electron transfer to dioxygen,  $O_2$ , to form superoxide,  $O_2^{\cdot-}$ . Finally, we observe a decrease in the limiting current density for oxygen reduction with increasing pH in the RRDE experiments. In combination, these two observations point towards an oxygen reduction mechanism that involves an initial outer-sphere reduction of oxygen to superoxide followed by disproportionation. As demonstrated previously for metal-free carbon electrodes by Yang and McCreery,<sup>36</sup> the decreasing limiting current density is consistent with disproportionation of the superoxide intermediate to form  $O_2$  and hydro(gen) peroxide. Together, all these observations guide us towards modeling oxygen reduction on this material via an EC'D mechanism.

### *EC'D mechanism*

In the EC'D mechanism shown in Reactions [4-6], an electrochemical reaction (E) converts the neutral polymer,  $N$ , into its reduced electron polaronic state,  $P$ . The polymer, now doped with reactive electrons, then chemically reacts with  $O_2$  to form superoxide,  $O_2^{\cdot-}$ , regenerating the neutral state of the polymer (C'). Superoxide radicals then disproportionate into  $O_2$  and hydro(gen) peroxide (D).



Note that step 3 can produce either hydrogen peroxide ( $\text{H}_2\text{O}_2$ ) or hydroperoxide ( $\text{HO}_2^-$ ) depending on the pH of the electrolyte (at  $\text{pH} < \text{p}K_{a,\text{H}_2\text{O}_2}$   $x = 2$ ; at  $\text{pH} > \text{p}K_{a,\text{H}_2\text{O}_2}$   $x = 1$ ):



A schematic of the reaction mechanism is shown in Figure S16:

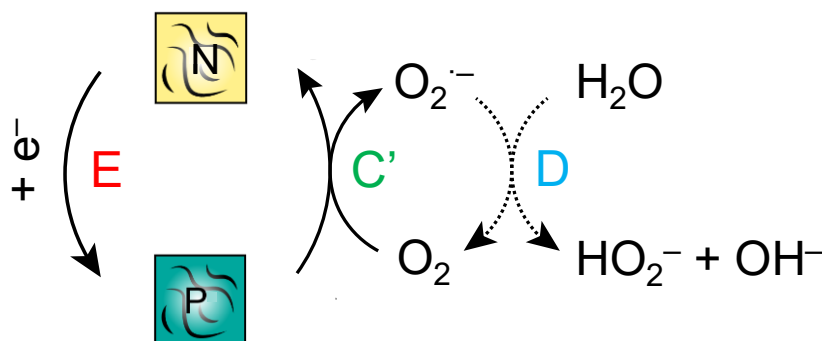


Figure S16. Schematic of the EC'D mechanism of oxygen reduction on p(NDI-T2 P75) at  $\text{pH} > \text{p}K_{a,\text{H}_2\text{O}_2}$ . The dotted arrows in step (D) demonstrate only a fraction of the superoxide is disproportionated into  $\text{O}_2$  and  $\text{HO}_2^-$ .

Because the DFT calculations showed no preference for adsorption of the superoxide intermediate, we consider electron transfer to oxygen intermediates to occur through outer sphere pathways defined by their thermodynamically reversible voltages. In an outer sphere process, the reduction of dissolved  $\text{O}_2$  to form superoxide,  $\text{O}_2^-$ , occurs at a reversible potential of  $E_{\text{O}_2/\text{O}_2^-}^{0'} = -0.16 \text{ V vs. SHE}$ .<sup>34,35</sup> Note that this reduction voltage is pH invariant above the  $\text{p}K_a$  of  $\text{HO}_2$  ( $\text{p}K_{a,\text{HO}_2} = 4.88$ ).

The net hydrogen peroxide production reaction has a standard reduction voltage of  $E_{\text{O}_2/\text{H}_2\text{O}_2}^0 = 0.695 \text{ V vs. SHE}$ .<sup>37</sup> The formal (reversible) reduction voltage (vs. SHE),  $E_{\text{O}_2/\text{H}_x\text{O}_2}^{0'}$ , can be calculated using Equation [8], where  $F$  is Faraday's constant,  $R$  is the ideal gas constant, and  $T$  is the absolute temperature (298.15K in this case):

$$E_{\text{O}_2/\text{H}_x\text{O}_2}^{0'} = E_{\text{O}_2/\text{H}_2\text{O}_2}^0 - \frac{2.303RT}{2F} [(2-x) \text{p}K_{a,\text{H}_2\text{O}_2} + (x)\text{pH}] \quad [8]$$

The formal reduction voltage of the electron polaron reaction,  $E_1^{0'}$ , can be measured directly or calculated as a fitting parameter in the model. Here, we fit this parameter to test the validity of the proposed model.  $K_2$  and  $K_3$ , the equilibrium constants for the chemical reactions in Steps 2 and 3 can be evaluated as, where  $f = \frac{F}{RT}$ :

$$K_2 = \exp[f(E_{O_2/O_2^-}^0 - E_1^{0'})] \quad [9]$$

$$K_3 = \exp[f(E_{O_2/H_xO_2}^{0'} - 2E_{O_2/O_2^-}^{0'})] \quad [10]$$

At pH 14.2, the highest pH in this study,  $K_3$  has a value of  $1.6 \times 10^4$  suggesting only the forward direction of Reaction [6] needs to be considered.

Reactions [4-6] are cast into a set of rate expressions, where  $k_i^*$  is an electrochemical rate coefficient (dependent on applied voltage),  $k_i$  is a chemical rate coefficient (independent of applied voltage),  $\theta_N$  and  $\theta_P$ , are the surface fractions of the polymer in its neutral and electron polaron states, respectively, and  $C_a^s$  is the concentration of species  $a$  at the surface of the electrode:

$$v_1 = k_{f,1}^* \theta_N - k_{b,1}^* \theta_P \quad [11]$$

$$v_2 = k_{f,2} \theta_P C_{O_2}^s - k_{b,2} C_{O_2}^s \theta_N \quad [12]$$

$$v_3 = k_{f,3} C_{O_2}^{s-2} \quad [13]$$

Mass transfer of species in solution is treated as linear across the diffusion layer. Under the Levich model for a rotating disk electrode (RDE), the diffusion layer thickness for species  $a$ ,  $\delta_a$ , is dependent on the rotation rate of the electrode,  $\omega$ , the diffusion rate of species  $a$ ,  $D_a$ , and the kinematic viscosity of the electrolyte,  $\nu = 0.01 \text{ cm}^2 \text{ s}^{-1}$  for  $[K^+] = 1 \text{ M}$  aqueous electrolytes.<sup>38</sup>

$$\delta_a = 1.61 D_a^{1/3} \omega^{-1/2} \nu^{1/6} \quad [14]$$

The diffusion rate of  $O_2$  in the electrolyte,  $D_{O_2} = 1.9 \times 10^{-5} \text{ cm}^2 \text{ s}^{-1}$ , was used for all pH, which was estimated from the limiting current of a Pt electrode tested in the same pH electrolytes (Figure S6). We assume the diffusion rate of  $O_2^-$  is the same as  $O_2$ .

The mass transfer coefficient,  $m_a$ , is the ratio of the diffusion rate to the diffusion layer thickness:

$$m_a = \frac{D_a}{\delta_a} \quad [15]$$

Because the electrochemical data is obtained at a scan rate of  $0.5 \text{ mV s}^{-1}$ , we can reasonably assume the system is at steady-state. We thus use the steady-state approximation to solve the

system of equations [11-13, 16-19], where  $C_a^b$  is the bulk concentration of species  $a$  far away from the electrode surface ( $C_{O_2}^b = 0.8 \text{ mM}$ ).<sup>39</sup>

$$D_{O_2} \left( \frac{\partial C_{O_2}}{\partial x} \right) = m_{O_2} (C_{O_2}^b - C_{O_2}^s) = v_2 - v_3 \quad [16]$$

$$D_{O_2^-} \left( \frac{\partial C_{O_2^-}}{\partial x} \right) = -m_{O_2} C_{O_2}^s = 2v_3 - v_2 \quad [17]$$

$$\frac{d\theta_P}{dt} = v_1 - v_2 = 0 \quad [18]$$

$$\theta_N + \theta_P = 1 \quad [19]$$

The electrochemical rate coefficients are calculated using the Butler-Volmer equation, where  $E_i^{0'}$  is the formal (reversible) reduction voltage based on the pH and reaction conditions,  $\beta_i$  is the symmetry coefficient, and  $k_i^0$  is the rate constant at zero overvoltage for reaction  $i$ :

$$k_{f,i}^* = k_i^0 \exp[-\beta_i f(E - E_i^{0'})] \quad [20]$$

$$k_{b,i}^* = k_i^0 \exp[(1 - \beta_i) f(E - E_i^{0'})] \quad [21]$$

The chemical rate coefficients are constant at all pH's, where the backwards rate coefficient is defined by the equilibrium constant for reaction  $i$ :

$$k_{b,i} = \frac{k_{f,i}}{K_i} \quad [22]$$

The disk current density,  $j_{RRDE,disk}^{model}$ , corresponds only to reactions where net electrons are transferred to/from the external circuit. In this case, the only electrochemical reaction is the reduction of the neutral polymer to its polaronic state in Reaction [4].

$$j_{RRDE,disk}^{model} = -Fv_1 \quad [23]$$

Although the experimental ring current was not used in the fit, we can simulate this current,  $j_{RRDE,ring}^{model}$ , through Equation [24] which accounts for the number of number of electrons involved in the oxidation of hydro(gen) peroxide ( $n = 2$ ) and the collection efficiency of the ring electrode ( $N_{eff} = 0.25$ ):

$$j_{RRDE,ring}^{model} = 2N_{eff}Fv_3 \quad [24]$$

We also fit the mass transfer corrected experimental Tafel data,  $j_{kinetic}^{exp}$ , to a kinetic form of the simulation,  $j_{kinetic}^{model}$ , which does not consider the effects of mass transfer. To remove the effects of mass transfer in the simulation, we set  $m_{O_2}$  to an arbitrarily high value of  $10^6 \text{ cm s}^{-1}$  (effectively a rotation rate of  $\omega \approx 1 \times 10^6 \text{ r.p.m.}$ ) in Equation [16]. Finally, we additionally use the local Tafel slope,  $b$ , to help constrain the fit:

$$b = \frac{\partial \log j_{kinetic}^{model}}{\partial E} \quad [25]$$

We fit the experimental pH-dependent normalized RDE and Tafel data using a self-consistent set of 4 pH-independent parameters,  $E_1^{0'}$ ,  $k_1^0$ ,  $\beta_1$ ,  $k_{f,2}$ , and treat  $k_{f,3}$  as pH dependent (each experimental pH has its own independent  $k_{f,3}$  fit). The fitted parameters are presented in Table 1 of the main text and the total root mean square error for all fits was  $R = 0.085$ . The results of the simulation are presented in Figure 6 in the main text.

In Figure 6c in the main text, the fitted  $E_1^{0'}$  values are shown as dotted lines overlaying the experiment cyclic voltammograms of  $p(\text{NDI-T2 P75})$  in Ar-saturated electrolytes. We find that the fitted  $E_1^{0'}$  values show excellent agreement with the observed  $E_{1/2}$  of the second polaron peak, which supports the hypothesized reaction EC'D mechanism. This reaction has a standard rate coefficient of  $k_1^0 = 1.24 \times 10^{-6} \text{ mol cm}^{-2} \text{ s}^{-1}$ . Although it is difficult to directly measure the surface reaction site density of the polymer,  $\Gamma_{geo}$ , we approximate it as the total loading of polaronic sites on the electrode, assuming one polaron per (NDI-T2 P75) repeat unit, where  $MW$  is the molar mass of the repeat unit ( $W = 1052.25 \text{ g mol}^{-1}$ ) and  $\rho$  is the density of the dry polymer ( $\rho = 0.9 \text{ g cm}^{-3}$ ).

$$\Gamma_{geo} = \frac{\rho}{W} \quad [26]$$

Then, assuming all reaction sites are active, we can calculate the standard heterogeneous rate coefficient as  $k_1^{0'} = 1.44 \times 10^{-3} \text{ cm s}^{-1}$  through Equation [27]:

$$k_1^{0'} = \frac{k_1^0}{\Gamma_{geo}} \quad [27]$$

Comparing  $k_1^{0'}$  to  $k_{f,2}$ , it is clear that polaron formation is the rate-limiting step (RLS) of superoxide generation, which helps to explain the experimental observation of polaron

suppression, whereby oxygen rapidly oxidizes any polaron formed through the chemical reaction in Reaction [5].

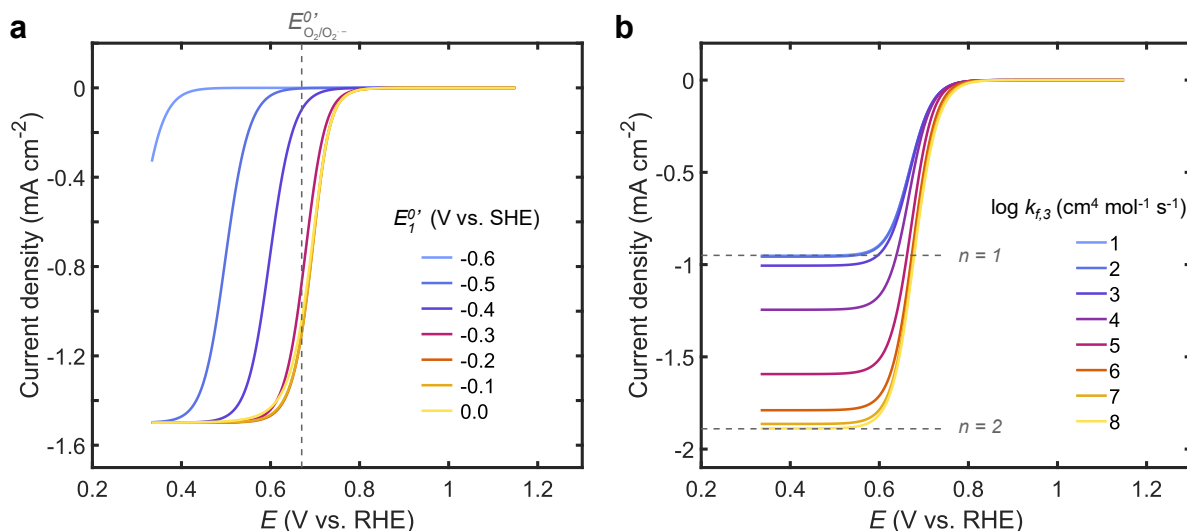


Figure S17. Effects of **a)**  $E_1^{0'}$  and **b)**  $k_{f,3}$  on the ORR at pH 14.2. For each simulation, all other parameters were held constant and correspond to the values in Table 1 for pH 14.2. In (b), the dotted lines correspond to the expected limiting current densities from the Levich equation for an  $n = 1$  and  $n = 2$  reduction of oxygen.

In Figure S17, we demonstrate the effects of the polaron formation voltage,  $E_1^{0'}$ , and the superoxide disproportionation rate,  $k_{f,3}$ , at pH 14.2. The practical effects of  $E_1^{0'}$  can be observed in Figure 7 in the main text, where n-type polymers with more negative polaron formation voltages (i.e. p(gPyDPP-MeOT2)) have more negative halfwave voltages for oxygen reduction and polymers with more positive polaron formation voltages (i.e. p(NDI-T)) have a halfwave voltage for oxygen reduction that is pinned by the outer-sphere formal reduction potential for the  $O_2/O_2^-$  redox couple,  $E_{O_2/O_2^-}^{0'}$ , which becomes the rate-limiting step in oxygen reduction.

As discussed in the main text, Figure S17b demonstrates that the disproportionation rate,  $k_{f,3}$ , primarily affects the limiting current densities but not the halfwave voltage of oxygen reduction, where low disproportionation rates result in superoxide formation ( $n=1$ ) while high disproportionation rates push the electron transfer number towards  $n = 2$  due to the feedback loop of generated  $O_2$ . Catalytic disproportionation of superoxide can help to explain the differences in oxygen reduction performance between p(NDI-T2 P75) and bare glassy carbon seen in Figure 7 in the main text. While bare glassy carbon shares the same halfwave voltage as p(NDI-T2 P75), it only generates half of the limiting current in 0.1 M KOH. Indeed, the shape of the current-voltage relationship on glassy carbon has been explained through buildup of

superoxide<sup>40</sup> in alkaline solutions, where homogeneous disproportionation is expected to have a rate constant of  $k_{obsd} \approx 0.5 \text{ M}^{-1} \text{ s}^{-1}$  resulting in a 10% decrease in superoxide concentration requiring  $\sim 3 \text{ min}$  for a 1 mM concentration of dissolved  $\text{O}_2$ .<sup>40,41</sup>

In summary, our microkinetic simulation helps to explain the oxygen reduction activity of OMIEC electrodes through EC'D mechanism. For polymers with  $E_1^{0'} < E_{\text{O}_2/\text{O}_2^-}^{0'}$ , the rate of oxygen reduction is limited by the rate of polymer reduction whereby the slower formed polaronic state is rapidly consumed (and thereby suppressed) by a chemical reaction with oxygen to form superoxide. Polymers with  $E_1^{0'} > E_{\text{O}_2/\text{O}_2^-}^{0'}$  can bypass the chemical step where oxygen reduction to superoxide then becomes rate-limiting. In all cases, the formed superoxide may be catalytically disproportionated by the polymers into  $\text{O}_2$  and  $\text{H}_x\text{O}_2^{(2-x)}$  at a rate that decreases with increasing pH. The  $\text{O}_2$  formed through disproportionation then feeds back into the reaction cycle to chemically consume the polaron leading to a variation in the observed limiting current that scales with the disproportionation rate. On glassy carbon, which is non-catalytic for superoxide disproportionation, the half-wave voltage occurs at  $E_{\text{O}_2/\text{O}_2^-}^{0'}$  and the limiting current density corresponds to a single electron transfer to form superoxide which builds up at the electrode surface causing a decrease in current density with increasing potential.

## Section 10. Testing an NDI-T2 copolymer with nonpolar sidechains

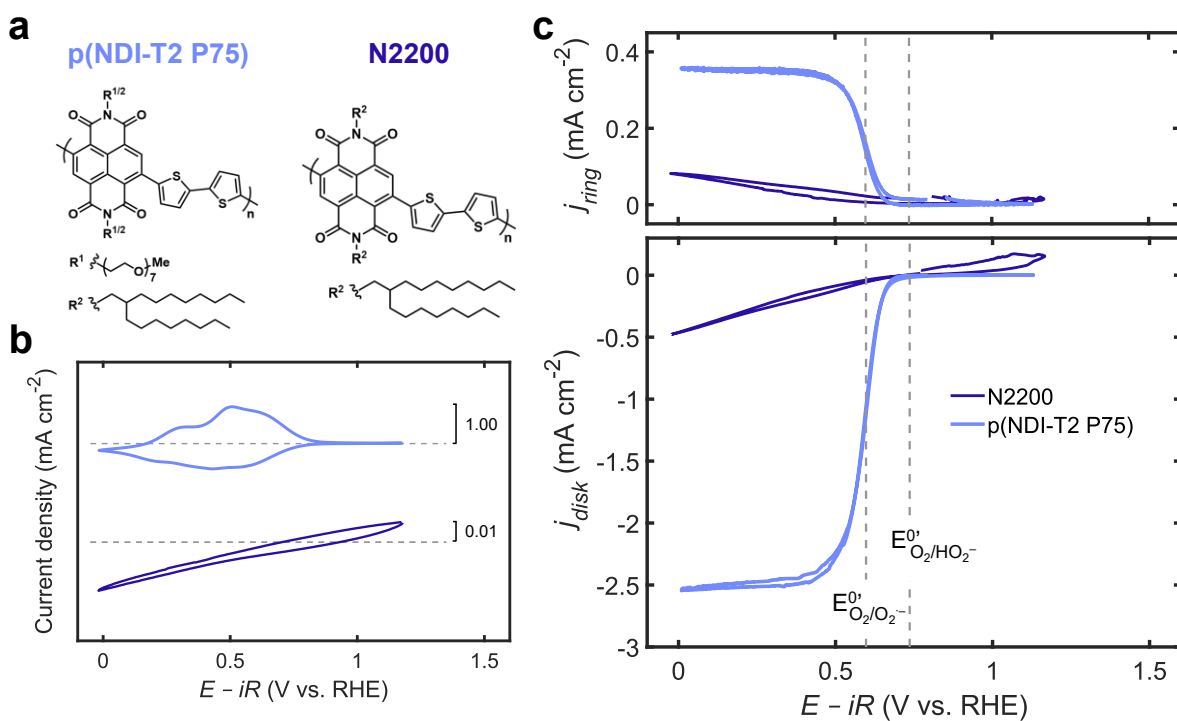


Figure S18. **a**) Structures of p(NDI-T2 P75) and N2200. **b**) Ar saturated bulk cyclic voltammograms in 0.1 M KOH at a scan rate of 5 mV s<sup>-1</sup>. **c**) RRDE measurements in O<sub>2</sub> saturated 0.1 M KOH at 1600 rpm at a scan rate of 0.5 mV s<sup>-1</sup>.

## References

- 1 A. T. Murray, S. Voskian, M. Schreier, T. A. Hatton and Y. Surendranath, *Joule*, 2019, **3**, 2942–2954.
- 2 J. M. Campos-Martin, G. Blanco-Brieva and J. L. G. Fierro, *Angewandte Chemie International Edition*, 2006, **45**, 6962–6984.
- 3 W. Zhou, X. Meng, J. Gao and A. N. Alshwabkeh, *Chemosphere*, 2019, **225**, 588–607.
- 4 K. Jiang, J. Zhao and H. Wang, *Adv Funct Mater*, 2020, **30**, 2003321.
- 5 Z. Wang, Q.-K. Li, C. Zhang, Z. Cheng, W. Chen, E. A. McHugh, R. A. Carter, B. I. Yakobson and J. M. Tour, *ACS Catal*, 2021, **11**, 2454–2459.
- 6 H. Hou, X. Zeng and X. Zhang, *Angewandte Chemie International Edition*, 2020, **59**, 17356–17376.
- 7 Y. Wang, G. I. N. Waterhouse, L. Shang and T. Zhang, *Adv Energy Mater*, 2021, **11**, 2003323.
- 8 M. L. Pegis, C. F. Wise, D. J. Martin and J. M. Mayer, *Chem Rev*, 2018, **118**, 2340–2391.
- 9 W. R. P. Barros, Q. Wei, G. Zhang, S. Sun, M. R. V. Lanza and A. C. Tavares, *Electrochim Acta*, 2015, **162**, 263–270.
- 10 J. F. Carneiro, L. C. Trevelin, A. S. Lima, G. N. Meloni, M. Bertotti, P. Hammer, R. Bertazzoli and M. R. v. Lanza, *Electrocatalysis*, 2017, **8**, 189–195.
- 11 R. Gao, L. Pan, Z. Li, C. Shi, Y. Yao, X. Zhang and J. Zou, *Adv Funct Mater*, 2020, **30**, 1910539.
- 12 H. Sheng, E. D. Hermes, X. Yang, D. Ying, A. N. Janes, W. Li, J. R. Schmidt and S. Jin, *ACS Catal*, 2019, **9**, 8433–8442.
- 13 K. Jiang, S. Back, A. J. Akey, C. Xia, Y. Hu, W. Liang, D. Schaak, E. Stavitski, J. K. Nørskov, S. Siahrostami and H. Wang, *Nat Commun*, 2019, **10**, 3997.
- 14 Y. Wang, R. Shi, L. Shang, G. I. N. Waterhouse, J. Zhao, Q. Zhang, L. Gu and T. Zhang, *Angewandte Chemie International Edition*, 2020, **59**, 13057–13062.
- 15 R. Cao, J.-S. Lee, M. Liu and J. Cho, *Adv Energy Mater*, 2012, **2**, 816–829.
- 16 X. Hu, X. Zeng, Y. Liu, J. Lu and X. Zhang, *Nanoscale*, 2020, **12**, 16008–16027.
- 17 Y. Bu, Y. Wang, G. Han, Y. Zhao, X. Ge, F. Li, Z. Zhang, Q. Zhong and J. Baek, *Advanced Materials*, 2021, **33**, 2103266.
- 18 H. W. Kim, M. B. Ross, N. Kornienko, L. Zhang, J. Guo, P. Yang and B. D. McCloskey, *Nat Catal*, 2018, **1**, 282–290.
- 19 H. W. Kim, V. J. Bukas, H. Park, S. Park, K. M. Diederichsen, J. Lim, Y. H. Cho, J. Kim, W. Kim, T. H. Han, J. Voss, A. C. Luntz and B. D. McCloskey, *ACS Catal*, 2020, **10**, 852–863.

- 20 E. J. Askins, M. R. Zoric, M. Li, Z. Luo, K. Amine and K. D. Glusac, *Nat Commun*, 2021, **12**, 3288.
- 21 G.-F. Han, F. Li, W. Zou, M. Karamad, J.-P. Jeon, S.-W. Kim, S.-J. Kim, Y. Bu, Z. Fu, Y. Lu, S. Siahrostami and J.-B. Baek, *Nat Commun*, 2020, **11**, 2209.
- 22 Y. Wang, J. Le, W. Li, J. Wei, P. M. Radjenovic, H. Zhang, X. Zhou, J. Cheng, Z. Tian and J. Li, *Angewandte Chemie International Edition*, 2019, **58**, 16062–16066.
- 23 P. M. Radjenovic and L. J. Hardwick, *Physical Chemistry Chemical Physics*, 2019, **21**, 1552–1563.
- 24 X. Li and A. A. Gewirth, *J Am Chem Soc*, 2005, **127**, 5252–5260.
- 25 P. Adler, P. Jeglič, M. Reehuis, M. Geiß, P. Merz, T. Knaflič, M. Komelj, A. Hoser, A. Sans, J. Janek, D. Arčon, M. Jansen and C. Felser, *Sci Adv*, , DOI:10.1126/sciadv.aap7581.
- 26 X. Li and A. A. Gewirth, *J Am Chem Soc*, 2005, **127**, 5252–5260.
- 27 J. Wei, D. Xia, Y. Wei, X. Zhu, J. Li and L. Gan, *ACS Catal*, 2022, **12**, 7811–7820.
- 28 Y.-L. Sun, Y.-L. A, M.-F. Yue, H.-Q. Chen, H. Ze, Y.-H. Wang, J.-C. Dong, Z.-Q. Tian, P.-P. Fang and J.-F. Li, *Anal Chem*, 2022, **94**, 4779–4786.
- 29 J.-C. Dong, M. Su, V. Briega-Martos, L. Li, J.-B. Le, P. Radjenovic, X.-S. Zhou, J. M. Feliu, Z.-Q. Tian and J.-F. Li, *J Am Chem Soc*, 2020, **142**, 715–719.
- 30 I. C. Man, H. Su, F. Calle-Vallejo, H. A. Hansen, J. I. Martínez, N. G. Inoglu, J. Kitchin, T. F. Jaramillo, J. K. Nørskov and J. Rossmeisl, *ChemCatChem*, 2011, **3**, 1159–1165.
- 31 N. Siemons, D. Pearce, C. Cendra, H. Yu, S. M. Tuladhar, R. K. Hallani, R. Sheelamanthula, G. S. LeCroy, L. Siemons, A. J. P. White, I. Mcculloch, A. Salleo, J. M. Frost, A. Giovannitti and J. Nelson, .
- 32 B. B. Blizanac, P. N. Ross and N. M. Markovic, *Electrochim Acta*, 2007, **52**, 2264–2271.
- 33 M. Schalenbach, *Int J Electrochem Sci*, 2018, 1173–1226.
- 34 P. M. Wood, *Biochemical Journal*, 1988, **253**, 287–289.
- 35 W. H. Koppenol, D. M. Stanbury and P. L. Bounds, *Free Radic Biol Med*, 2010, **49**, 317–322.
- 36 H.-H. Yang and R. L. McCreery, *J Electrochem Soc*, 2000, **147**, 3420.
- 37 D. A. Armstrong, R. E. Huie, S. Lyman, W. H. Koppenol, G. Merényi, P. Neta, D. M. Stanbury, S. Steenken and P. Wardman, *Bioinorg React Mech*, , DOI:10.1515/irm-2013-0005.
- 38 P. Singh and D. A. Buttry, *The Journal of Physical Chemistry C*, 2012, **116**, 10656–10663.
- 39 X.-Z. Yuan, X. Li, W. Qu, D. G. Ivey and H. Wang, *ECS Trans*, 2011, **35**, 11–20.
- 40 J. R. Strobl, N. S. Georgescu and D. Scherson, *Electrochim Acta*, 2020, **335**, 135432.

41 V. F. Mattick, X. Jin, R. E. White and K. Huang, *J Electrochem Soc*, 2020, **167**, 124518.